Scientific Reports

https://doi.org/10.1038/s41598-026-45242-5

Article in Press

Study on the influence of key parameters of sand emission on dust flux based on multi-source data

Received: 18 December 2025

Accepted: 17 March 2026

Published online: 26 March 2026

Cite this article as: Maihamuti M., Huo W., Liu Y. *et al.* Study on the influence of key parameters of sand emission on dust flux based on multi-source data. *Sci Rep* (2026). https://doi.org/10.1038/s41598-026-45242-5

Mayibaier Maihamuti, Wen Huo, Yongqiang Liu, Yifei Wang, Fan Yang, Chenglong Zhou, Xinghua Yang, Ali Mamtimin & Mierxiatijiang Maihemuti

Study on the Influence of Key Parameters of Sand Emission on Dust Flux Based on Multi-source Data

Mayibaier Maihamuti[1,2,3,4,5], Wen Huo[2,3,4,5]*, Yongqiang Liu[1,2,3,4,5]*, Yifei Wang[1,2,3,4,5] , Fan Yang[2,3,4,5], Chenglong Zhou[2,3,4,5], Xinghua Yang[2,3,4,5,6], Ali Mamtimin[2,3,4,5], Mierxiatijiang Maihemuti[7]

1. College of Geography and Remote Sensing Sciences, Xinjiang University, Urumqi 830046, China

2. Institute of Desert Meteorology, China Meteorological Administration, Urumqi 830002, China

3. National Observation and Research Station of Desert Meteorology, Taklimakan Desert of Xinjiang, Urumqi 830002, China

4. Taklimakan Desert Meteorology Field Experiment Station, China Meteorological Administration, Urumqi 830002, China

5. Xinjiang Key Laboratory of Desert Meteorology and Sandstorm, Urumqi 830002, China

6. School of Geographical Sciences, Shanxi Normal University, Taiyuan 030032, Shanxi, China

7. China Merchants Xinjiang Quality and Standardization Research Institute Co., Ltd.Urumqi 830011,China

* Corresponding authors: huowenpet@idm.cn, lyqxju@163.com

Abstract: This study analyzes ground-based observations and multi-source remote sensing data from eight dust storm events in 2024 at two sites: the Tazhong (TZ) station in the Taklamakan Desert interior and the Xiaotang (XT) station on its northern margin, systematically investigates the interrelationships among dust particle size, friction velocity (U*), and dust flux, and evaluates the applicability of remote sensing data in dust monitoring. The results indicate that particle size significantly influences both horizontal fluxes (Q) and vertical dust fluxes (F). Fine particles (d[0.5]) enhance surface dust flux, while coarse particles (D[4,3])—due to their greater gravitational settling—are less capable of sustained suspension, limiting their long-distance transport. A positive correlation exists between friction velocity (U*) and Q, whereas its impact on F is weaker, suggesting that vertical transport is regulated primarily by particle size, gravitational settling, and turbulent structures. Regarding remote sensing data, MODIS Aerosol Optical Depth (AOD) shows strong consistency with ground-based dust flux measurements, especially at the Xiaotang (XT) station, where AOD closely follows the variation trends of both Q and F. This reflects the effectiveness of remote sensing data in capturing changes in dust activity. Additionally, the Aerosol Absorbing Index (AAI) from Sentinel-5P exhibits a highly significant positive correlation with ground-level dust concentrations, effectively reflecting the vertical structure of dust events. This research provides valuable data support and theoretical foundation for dust warning systems and desertification control projects.

Keywords: Dust flux; Particle size; Friction velocity; Multi-source remote sensing; Dust monitoring.

1 Introduction

Dust flux is a key parameter characterizing surface wind erosion and atmospheric dust transport, and serves as a core indicator in desertification monitoring and sandstorm early warning systems [1]. As a major arid region in inland Asia, the Taklamakan Desert is not only the largest mobile desert in China but also one of the primary source areas for dust aerosols in the mid-latitudes of the Northern Hemisphere [2]. Dust particles emitted from this region, influenced by both westerly circulation and local atmospheric systems, can be transported to East Asia, the North Pacific, and even North America [3], significantly affecting regional air quality, radiative balance, and glacier melt processes [4,5].

Considerable progress has been made in recent decades in characterizing dust emissions at desert margins and individual sites [6] , providing a foundation for understanding wind erosion dynamics.. However, due to the logistical challenges of conducting observations in the extreme environment of the desert hinterland, systematic comparisons between emission mechanisms in the interior versus marginal areas remain limited [7]. It is well established that dust emission is controlled by both the particle size distribution of surface sediments and near-surface aerodynamic conditions [8]. Nevertheless, the synergistic regulation of these factors on dust flux—particularly under conditions when friction velocity approaches or slightly exceeds the threshold friction velocity for particle entrainment—remains a major source of uncertainty in dust parameterization schemes [9]. In the Taklamakan Desert, Tazhong station (hinterland) and Xiaotang station (northern margin) represent typical high-intensity erosion and marginal transition zones, respectively [10]. While extensive observational data have been accumulated on wind erosion characteristics in each region [11]. comparative studies across sites remain rare, especially those integrating flux measurements with detailed particle size analysis [12]. Moreover, traditional dust flux estimates often rely on simplified parameters such as median particle diameter (D50) or a constant threshold friction velocity (U*) [13], potentially overlooking the differential erodibility represented by other particle size metrics (e.g., D[4,3] and d[0.5]), as well as nonlinear, threshold-dependent relationships between friction velocity and dust flux [14]. Addressing these gaps is essential for advancing physical understanding of wind erosion and improving dust emission models [15].

Recent advances in remote sensing offer new opportunities for dust flux studies through multi-source data integration [16]. For instance, aerosol optical depth (AOD) from MODIS provides information on the spatial and temporal evolution of dust plumes [17]，while the aerosol absorption index (AAI) from Sentinel-5P helps reveal the vertical distribution of dust aerosols [18]. However, linking satellite products to surface fluxes remains challenging due to mismatches in spatial resolution, cloud interference [19,20] and retrieval uncertainties [21–23]. AOD, as a column-integrated quantity, cannot distinguish near-surface emissions from elevated transport [24]; Sentinel-5P

offers higher resolution but has a longer revisit time, potentially missing localized erosion events [25]. Thus, developing robust spatiotemporal matching strategies and integrating ground-based and satellite observations are crucial steps toward improving dust flux inversion accuracy..

To address these issues, this study conducts a comparative analysis of dust emission mechanisms at Tazhong (hinterland) and Xiaotang (northern margin) stations in the Taklamakan Desert. By combining high-resolution ground-based measurements with multi-source satellite data, we aim to investigate: (1) how particle size characteristics influence horizontal and vertical dust fluxes; (2) the role of friction velocity in modulating dust emissions, particularly near threshold conditions; and (3) how remote sensing data can complement ground observations to reveal the spatiotemporal patterns of dust emission and transport. Through this integrated approach, we seek to elucidate differences in dust emission dynamics between the desert interior and its margin, thereby providing a physical basis for improving wind erosion models and supporting regional dust monitoring and early warning efforts.

2 Materials and Methods

2.1 Study Area

Taklimakan Desert is located in Tarim Basin, Xinjiang, China [26,27], it is the second largest mobile desert in the world, with a total area of about 350,000 square kilometers [28]. Surrounded by high mountains, the area is adjacent to Pamirs Plateau in the west, Kunlun Mountains in the south, Tianshan Mountains in the north and Lop Nur lowland in the east, forming a typical closed inland desert system [29]. The region experiences a hyper-arid continental climate, characterized by minimal annual precipitation—averaging only 75.00 mm—and high potential evaporation. Temperature extremes range from a minimum of −25 °C to a maximum of 40 °C, with pronounced diurnal variations. Persistent and strong winds, particularly during spring and early summer, drive frequent aeolian processes and sandstorm activity. The dominant soil types include saline soils, wind–sand soils, brown desert soils, and scrub desert soils [30] . Subject to arid climate conditions and strong wind activity, desert aeolian processes are frequent, making this region one of the most concentrated areas for dust storms in China. In some sections, the annual average number of dusty weather days can exceed 40 days [31]. The surface is predominantly covered by loose sandy sediments, with sparse or no vegetation cover, creating conditions highly susceptible to wind erosion [32]. This study focuses on selecting two representative observation sites within the Taklamakan Desert: the Tazhong Station (TZ) and the Xiaotang Station (XT), which respectively represent the typical aeolian environments of the desert interior and the transition zone at the desert's edge [33]. Tazhong Station is located in the central region of the desert (83°39′E, 38°58′N), with an elevation

of approximately 1,099 meters. The landscape is primarily characterized by longitudinal sand ridges and crescent-shaped dunes, with a topographic relief of 40–50 meters [33]. This region has favorable natural background conditions, making it an ideal monitoring area for analyzing the vertical structure evolution of dust and the characteristics of aeolian flux. Xiaotang Station (84° 18′E, 40°48′N, elevation 912 meters) is located at the northern edge of the desert, near the Tarim River and the distribution area of poplar forests, and is situated in the desert-oasis transition zone [34]. The site is surrounded by the remains of ancient channel landform, and the aeolian sand deposition and transportation are intertwined [35]. This site not only helps to capture the response characteristics of the marginal windblown environment, but also provides support for cross-validation of multi-source data for this study.

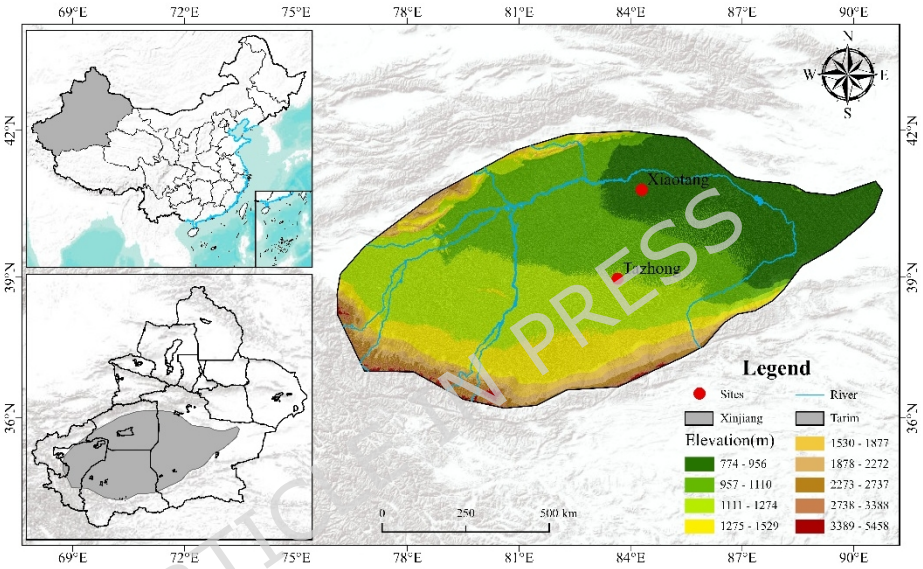

Figure 1. Overview of the Research Area

2.2 Observation Data and Experimental Design

The experimental workflow comprised three sequential phases: (1) an initial setup and pre-deployment phase, (2) a dust-event monitoring and sampling phase, and (3) a post-event retrieval and laboratory analysis phase.

2.2.1 Initial Setup and Pre-Deployment

Prior to each dust storm season, professionals inspected and cleaned the BSNE dust collection systems and sand traps at all observation heights (Table 1). All sampling bags were pre-weighed in the laboratory to avoid weight discrepancies caused by abrasion during transportation. All sampling personnel were qualified for high-altitude operations.

2.2.2 Dust-Event Sampling and Data Acquisition

Eight typical dust storm events were recorded simultaneously at both stations in 2024 (Table 2). During each event, the following protocol was followed:

1. Continuous monitoring: Near-surface micro-meteorological observation systems recorded wind speed, wind direction, atmospheric pressure, and temperature at multiple heights (1–100 m at XT; 1–80 m at TZ) throughout each dust storm..

2. Dust sampling: BSNE samplers at each height collected dust aerosol samples continuously during the event.[10].

Table 1. Taklamakan Desert Observation Station and Specifications Summary

Facility	Observation Height (m)
XT Station	1, 2, 4, 10, 24, 32, 47, 63, 80, 100
TZ Station	1, 2, 4, 8, 16, 24, 32, 47, 63, 80

2.2.3 Post-Event Retrieval and Laboratory Analysis

On the second day after each dust storm, when wind speeds fell below 5 m/s to ensure personnel safety, professionals retrieved dust samples from all heights, sealed them in pre-weighed bags, and transported them to the laboratory. In the laboratory, a laser particle size analyzer (Mastersizer Model 2000, Malvern, UK) was used to analyze the particle size distribution of the dust samples (measuring range: 0.02–2000 μm; error < 3%) [10].

Table 2. Start Times of Typical Dust Storm Events at Tazhong Station and Xiaotang Station in 2024 (UTC)

Dust Storm ID	Tazhong Station (TZ) Time	Xiaotang Station (XT) Time
Dust 1	2024-03-31 12:00	2024-03-31 12:00
Dust 2	2024-04-12 04:00	2024-04-12 04:00
Dust 3	2024-04-17 11:00	2024-04-17 11:00
Dust 4	2024-04-26 21:00	2024-04-26 21:00
Dust 5	2024-05-12 07:00	2024-05-12 07:00
Dust 6	2024-05-20 11:00	2024-05-20 11:00
Dust 7	2024-06-04 04:00	2024-06-04 04:00
Dust 8	2024-06-18 07:00	2024-06-18 07:00

2.2.4 Data Processing and Parameter Calculation

From the collected samples and meteorological data, key parameters were derived: horizontal dust flux (Q), vertical dust flux (F), and friction velocity (U*). The start times of the eight dust storm events (UTC) are summarized in Table 2. Vertical dust flux (F) was calculated using the gradient method [36–38] :

$$F = \rho U * \frac{(c_1 - c_2)}{\ln\left(\frac{z_2}{z_1}\right)} (1)$$

where F is the vertical dust flux (kg/m²); z_1 and z_2 are the measurement

heights (m); $U*$ is the friction velocity (m/s); c_1 and c_2 are the dust concentrations at the two measurement heights (kg/m³); k is the von Kármán constant (0.4), and $U*$ is the friction velocity (m/s). Concentration c was obtained from BSNE sediment samplers as:

$$c = \frac{M}{utA} (2)$$

Where M is the collected dust mass (kg), u is the mean wind speed during sampling (m/s), t is the sampling duration (s), and A is the inlet area of the sampler (m^2).

Computation of friction velocity u_*

The $U*$ in Eq.(1) is not a directly measured variable. It is calculated from two-level wind and temperature data using the Monin–Obukhov (M–O) similarity theory to account for atmospheric stability[39,40]:

$$\frac{kz}{U*}\frac{\partial u}{\partial z} = \varnothing_m(\zeta) (3)$$

where U is wind speed (m/s), $\varnothing_m(\zeta)$ is the dimensionless stability function, and ζ =z/L with L the M–O length. Integrating between the two observation levels and assuming $\varnothing_m$ is constant within this layer yields[41]

$$U(z_2) - U(z_1) = \frac{U*}{k}\phi_m(\zeta)\ln\frac{z_2}{z_1} (4)$$

from which

$$U* = \frac{k[U_2 - U_1]}{\phi_m(\zeta)\ln\left(\frac{z_2}{z_1}\right)} (5)$$

The stability function follows the Businger–Dyer formulation[42,43]:

$$\varnothing_m(\delta) = \begin{cases} (1 - 16\zeta)^{-0.25} & \zeta < 0 \text{ (unstable)} \\ (1 + 5\zeta) & \zeta \geq 0 \text{ (stable)} \end{cases} (6)$$

ζ is determined from the gradient Richardson number Ri[40]:

$$R_i = \frac{g\sqrt{z_1 z_2}}{\bar{T}}\frac{\Delta T}{(\Delta u)^2}\ln\left(\frac{Z_2}{Z_1}\right)$$

where $\bar{T}$ is the mean absolute temperature (K), ΔT =T2−T1, and ΔU=U2−U1. Then,

$$\zeta = \begin{cases} R_i & R_i < 0 \\ \dfrac{R_i}{1 - 5R_i} & R_i \geq 0 \end{cases} (5)$$

Thus, u_* used in Eq.(1) is obtained through Eqs.(3)–(4) with stability corrections before being applied to compute F. This approach avoids the bias

of a simple two-wind-speed estimate and clarifies that Eqs.(1) and (3) describe consistent stages of the same methodology.

2.3 Remote sensing data sources and processing methods

The remote sensing data used in this study primarily includes the aerosol optical depth (AOD) product retrieved from the MODIS (Moderate Resolution Imaging Spectroradiometer) sensor, as well as the aerosol absorption index (AAI) data provided by the Sentinel-5P satellite. All the data were processed and extracted using the Google Earth Engine (GEE) platform. For the MODIS AOD product, the joint product provided by the sensors onboard the Terra and Aqua satellites was selected (MODIS/061/MCD19A2_GRANULES). The spatial resolution of the data is 10 km, and the temporal resolution is daily. This resolution was chosen for two primary reasons: (1) it better matches the spatial footprint of dust transport inferred from the BSNE network, as point-based ground measurements are more representative of regional-scale dust flux when compared to 1 km retrievals that may capture local variability unrelated to synoptic dust events [48]; and (2) the 10 km product provides more continuous temporal coverage with fewer gaps due to cloud screening, which is particularly important in capturing the full duration of dust storms that evolve over multiple hours to days. While higher-resolution (1 km) AOD products are available, they are more susceptible to cloud contamination and surface reflectance heterogeneity in arid regions, potentially introducing noise in dust source areas. The data are sourced from the NASA LAADS DAAC data center (https://ladsweb.modaps.eosdis.nasa.gov). To improve the adaptability to the surface in arid regions, the Optical_Depth_047 band was extracted. In addition, high-quality pixels were selected by applying the quality assurance flag (QA_flag $\geq$ 2) to filter out low-quality data. This approach was used to minimize errors caused by cloud interference and high surface albedo.

The Sentinel-5P data is sourced from the European Space Agency (ESA) through the Copernicus program. The specific product used is the COPERNICUS / S5P /OFFL / L3 _ AER _ AI dataset, which can be found at https://developers.google.com/earth-engine datasets/catalog/COPERNICUS_S5P_OFFL_L3_AER_AI. This product has a spatial resolution of 7 km and a temporal resolution of daily scale. The data were processed through the GEE platform, with pixels severely affected by cloud interference removed. Only observations with good quality control were retained to ensure the reliability of the AAI values. AAI reflects the relative amount of absorbing aerosols in the atmosphere and can effectively identify strongly absorbing aerosols such as dust and smoke. In this study, to explore the relationship between near-surface dust concentration and column-integrated aerosol absorption characteristics, eight typical dust storm events from 2024 were selected. It is important to note that while AAI provides information on the presence of absorbing aerosols in the atmospheric column, it does not directly resolve the vertical distribution of dust. Therefore, this

analysis focuses on the correlation between surface-measured dust concentration and total-column AAI, rather than attempting to infer vertical structure from satellite data alone. The time range for extraction corresponds to the UTC duration of each event, and the spatial extraction range covers a 5 km radius around the Tazhong Station and Xiaotang Station. The AAI values were obtained using a time-averaging method.

2.4 Ground-Satellite Data Integration and Statistical Analysis

The ground-based observational data were obtained from an automatic dust monitoring system, which provided the horizontal dust flux (Q, in kg/m^2) at 10 different layers within the height range of 1–100 meters at XT Station and 1–80 meters at TZ Station, along with corresponding wind speeds (WS, in m/s) at each height. To estimate the dust concentration (C, in kg/m^3) at different heights, the following equation was used for calculation:

$$C = \frac{Q}{WS} \quad (6)$$

In this case, Q represents the dust flux at a specific height, and WS represents the horizontal wind speed at that height. The formula reflects the dust mass concentration transported by wind within a unit volume.

For each dust event, the average dust concentration at each height was paired with the corresponding satellite-derived AAI value. Pearson correlation coefficients (r) and significance levels (p-values) were calculated to assess the linear relationship between AAI and vertical dust concentration.. All data processing and visualization were conducted using Python. This integrated ground-satellite approach supports the application of remote sensing products in dust monitoring and provides a technical foundation for ground-satellite fusion research.

3 Results

3.1 Characteristics of Dust Events and Particle Size Effects on Dust Flux

In order to gain a deeper understanding of the impact of dust particle size on flux distribution, this section begins by examining the relationship between particle size parameters and flux at different heights. By combining the observational data from the TZ and XT stations, it analyzes the characteristics of horizontal dust flux (Q) and vertical flux (F) during eight dust events, with respect to changes in particle size and friction velocity (U*). This diversity in event characteristics provides a robust basis for examining the mechanisms controlling dust flux under different meteorological and surface conditions.

Figure 2-3 illustrates the relationship between two key particle size parameters—volume mean diameter (D[4,3]) and median diameter (d(0.5))—and horizontal dust flux (Q) and vertical flux (F) at different heights during eight dust storm events at the TZ and XT station. Figure 2(a-d) reveals that Q

generally exhibits a decreasing trend with increasing particle size, a pattern that becomes more pronounced at higher altitudes. At heights of 1 meter and 2 meters, D[4,3] and d(0.5) are smaller compared to upper layers, and the Q values are higher, indicating that smaller particles are more concentrated in the near-ground layer. As the height increases, the particle size gradually increases, and the concentration decreases, leading to a corresponding decrease in Q values. This trend is particularly pronounced during dust events with larger particle sizes (such as Dust 1 and Dust 8), where a clear negative correlation is observed between D[4,3] and Q. A comparison of the left and right charts shows that D[4,3] and d(0.5) are highly consistent in both magnitude and trend. Although there are differences in particle size and Q values across different dust events, the overall pattern remains consistent. The color variation indicates that when the particle size exceeds 80 μm, the decrease in Q with height becomes especially pronounced.

Figure 2(a-b) further illustrates the relationship between particle size (D[4,3] and d(0.5)) and vertical dust flux (F) at different height levels at the same location. The overall trend is consistent with that in Figure 2, with F decreasing as particle size increases. This is particularly evident in regions with larger D[4,3], where F decreases significantly, indicating that larger coarse particles (>80 μm) are more difficult to remain suspended at higher altitudes. In contrast, small particle size (<60 μm) is easier to be transported by high altitude and maintain higher concentration, resulting in larger F value. This trend is especially obvious at high altitude (e.g. 63m, 80m), dust concentration decreases rapidly, and particle size parameters become smaller. Event - to - event comparison of different processes also reveals that particle size distribution plays a dominant role in F value, for example, dust8 is dominated by large particle size and F value is lower, while dust1 is dominated by small particle size and F value is higher.

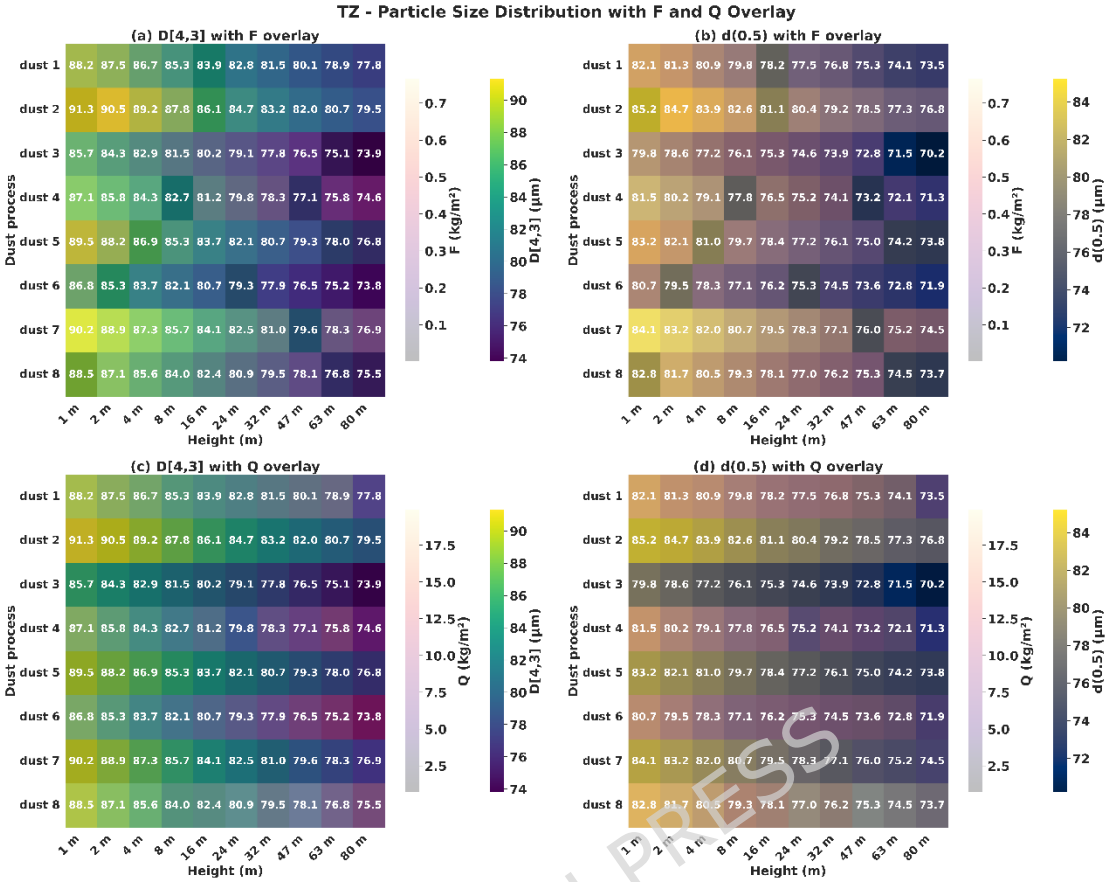

Figure 2. Relationship between dust particle size and dust flux at Tazhong (TZ).
(a) Volume mean diameter (D[4,3]) with vertical dust flux (F) overlay;
(b) Median diameter (d(0.5)) with vertical dust flux (F) overlay;
(c) Volume mean diameter (D[4,3]) with horizontal dust flux (Q) overlay;
(d) Median diameter (d(0.5)) with horizontal dust flux (Q) overlay.

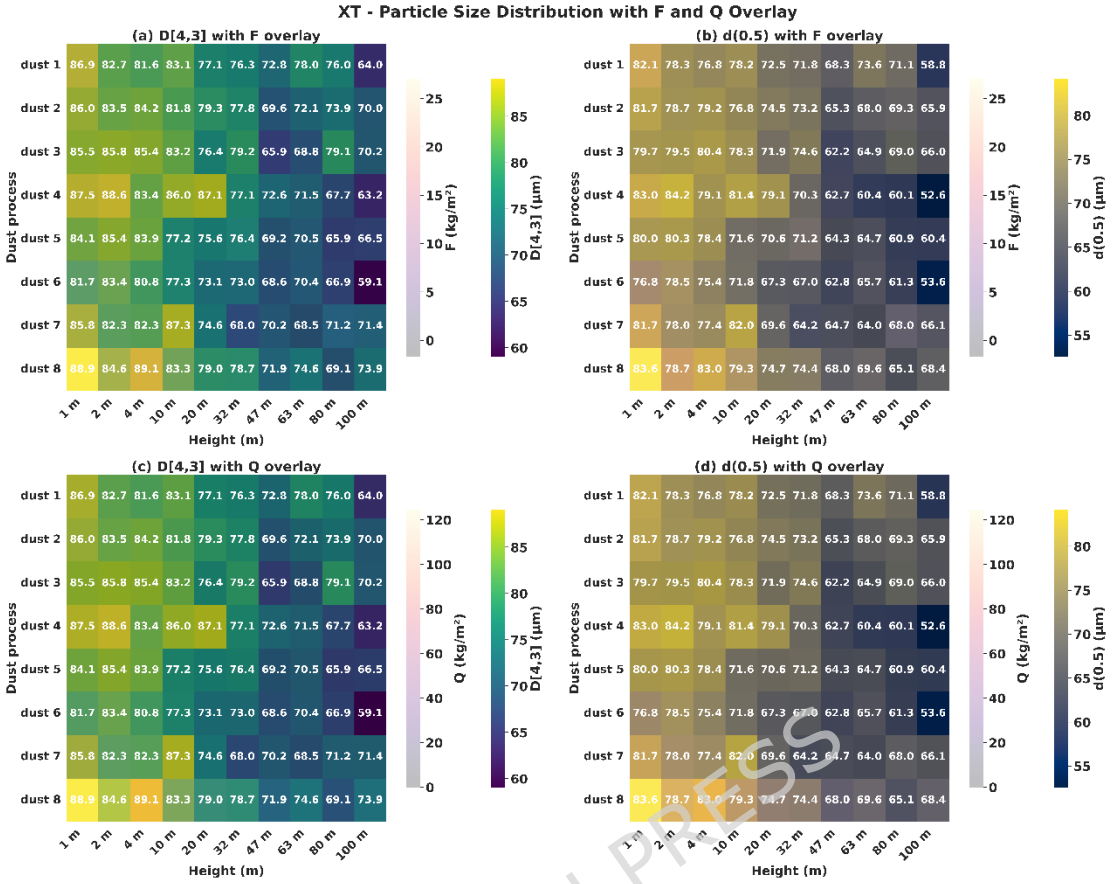

Figure 3. Relationship between dust particle size and dust flux at Xiaotang (XT).
(a) Volume mean diameter (D[4,3]) with vertical dust flux (F) overlay;
(b) Median diameter (d(0.5)) with vertical dust flux (F) overlay;
(c) Volume mean diameter (D[4,3]) with horizontal dust flux (Q) overlay;
(d) Median diameter (d(0.5)) with horizontal dust flux (Q) overlay.

Figure 3(a-d) shows the relationship between D[4,3], d(0.5), and Q at different height levels during various dust events at the XT station. The results indicate that Q increases as particle size decreases and decreases with increasing height. In the 1–4 m height range, particle sizes are generally larger than those at higher levels, and Q values are also higher, as seen in the initial stages of Dust 8 and Dust 4. As height increases, particle size decreases, and Q values drop rapidly, reflecting the larger proportion of fine particles at higher altitudes, yet the mass flux significantly decreases, which aligns with the theory of gravitational settling and turbulent diffusion. Especially between 80–100 meters in height, the particle size differences across various dust events become smaller, and Q values are generally lower. However, small changes in particle size near the surface correspond to significant differences in Q, indicating that lower-layer transport is more influenced by local factors such as topography and wind speed.

Figure 3(a-d) shows the relationship between particle size and vertical flux (F) at different heights during eight dust events at the XT station. Overall, F is negatively correlated with D[4,3], with F significantly decreasing when the

particle size exceeds approximately 80 μm, reflecting that coarse particles larger particles are more likely to settle. In contrast, smaller particles (<60 μm), due to their stronger suspension capability, lead to higher F values. The trend for d(0.5) is consistent with D[4,3], with smaller d(0.5) (around 60 μm) corresponding to higher concentrations, while larger particle sizes (such as 70 μm) correspond to lower concentrations. This trend is generally observed across all dust events and becomes more pronounced with increasing height, indicating that the vertical distribution is primarily controlled by particle size and gravitational settling.

3.2 Characteristics of U* Influence on Dust Flux

After analyzing the influence of dust particle size on dust flux distribution, this section will further explore the influence characteristics of friction velocity U* on dust flux, so as to deeply understand the mechanism of U* variation on dust horizontal and vertical transport.

Figure 4 illustrates the impact of friction velocity (U*) on Q and F during eight dust events at the TZ station. Overall, U* shows a strong positive correlation with Q. In most events (such as Dust 1 and Dust 4), as U* increases, Q clearly increases, suggesting that higher friction velocity helps to enhance the initiation and horizontal transport of surface particles. However, in events like Dust 2, Dust 6, and Dust 8, the response of Q to U* is less apparent, and in some cases, it even decreases slightly. This could be influenced by factors such as sand source depletion, surface humidity, particle size distribution, or local wind field structure. In contrast, U* has a weaker impact on F. In most dust events (such as Dust 2, 4, 6, and 8), F does not vary significantly with U*, and only in specific events like Dust 3 and Dust 5 is there a weak positive correlation. This indicates that F is more influenced by particle settling characteristics and gravity, with a relatively weak connection to wind speed variations.

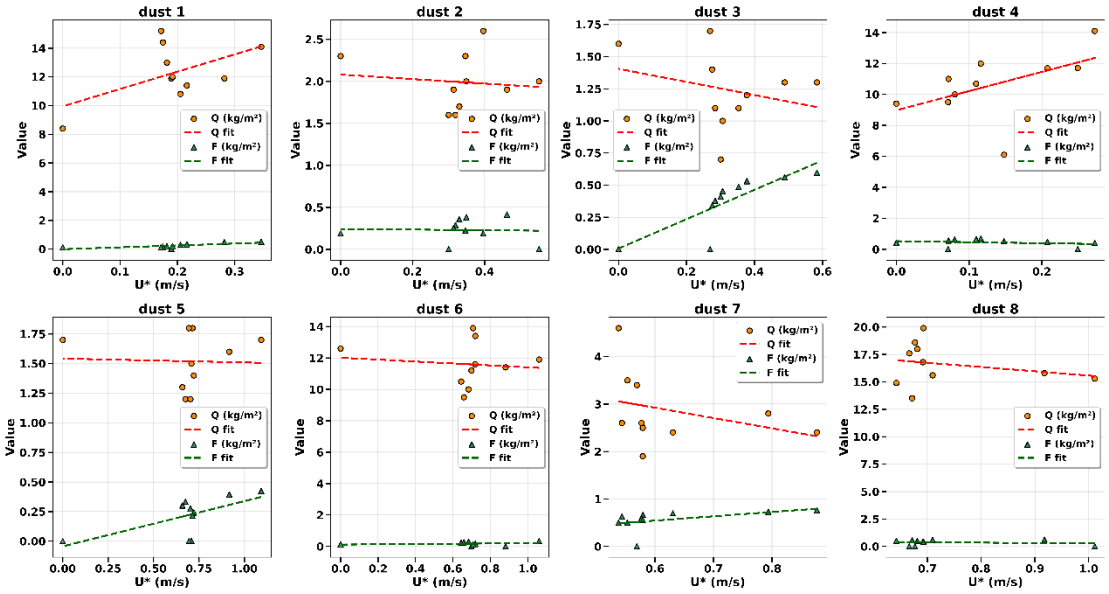

Figure 4. Variation of Q and F with U* under different dust processes in TZ

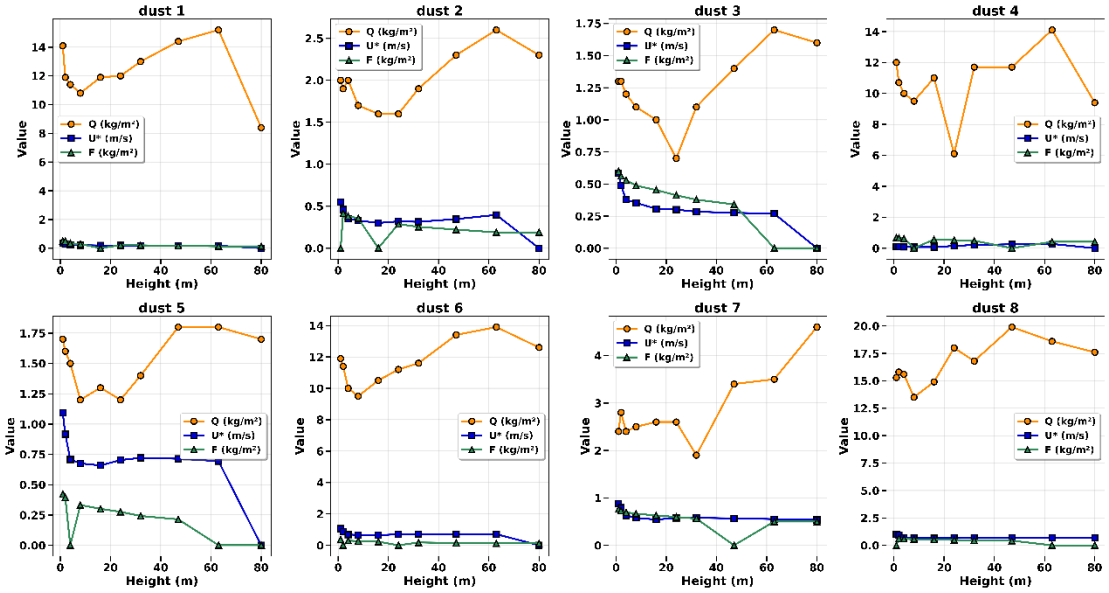

Figure 5. Vertical distribution characteristics of Q, F and U* under different dust processes in TZ

Figure 5 further illustrates the distribution characteristics of Q, F, and U* in the vertical direction. The results show that Q generally decreases with increasing height, indicating that strong winds can transport particles to higher altitudes, but the transport capacity gradually weakens with height. U* is typically larger near the surface and decreases with height, displaying typical characteristics of the friction layer. F is mainly concentrated in the lower layers and rapidly decays, reflecting that vertical flux primarily occurs near the ground surface. This also suggests that Q is more dependent on the driving force of lower-layer U*, while F is more controlled by particle size, gravitational settling, and vertical turbulent structures.

Figure 6 shows the relationship between Q and F with changes in U* at the XT station. Consistent with the TZ station, Q exhibits a positive correlation with U*, especially in Dust 1, 2, 6, and 7. However, the response of F to U* remains relatively weak, with only slight increases observed in a few events (such as Dust 1, 3, 6, and 7), but the increase is much smaller than that of Q. This further validates that friction velocity primarily drives horizontal transport processes, while its role in regulating vertical settling flux is limited.

Figure 7 shows the vertical distribution relationship between U* and Q, F at the XT station. The results indicate that although U* changes relatively steadily with height, its regulatory role in the sand transport process remains significant. At lower altitudes, larger U* contributes the most to Q, with Q values being significantly higher at lower heights and rapidly decreasing with height. In contrast, the vertical distribution of F is more complex, often exhibiting a peak at lower altitudes, followed by rapid decay or fluctuation. This reflects the nonlinear variation characteristics formed under the combined influence of particle size, gravity, and local turbulence.

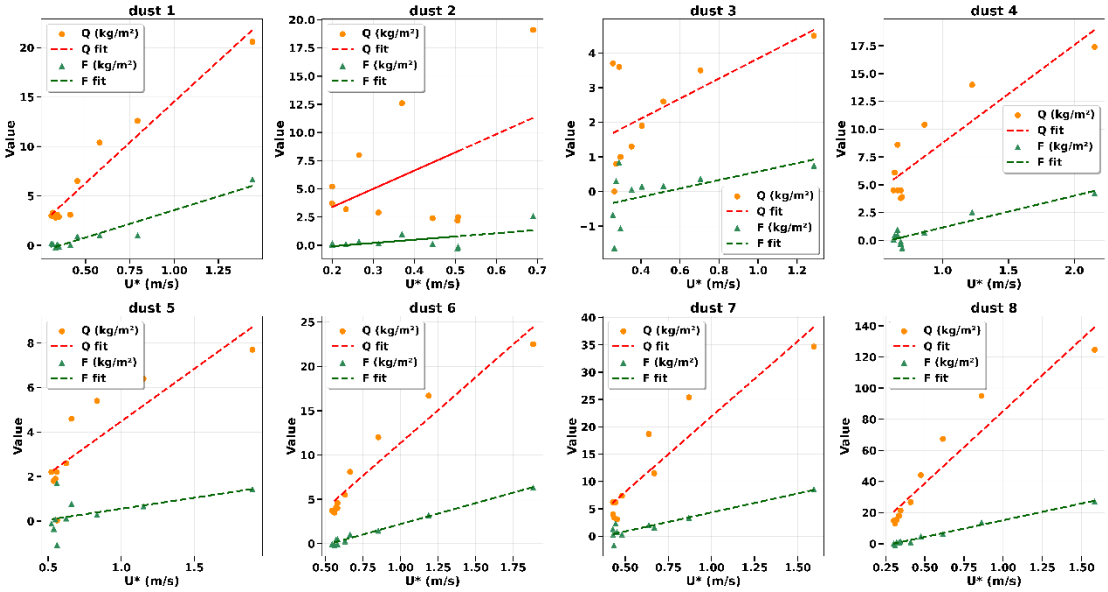

Figure 6. XT Relationship between Q and F and U* under different dust processes

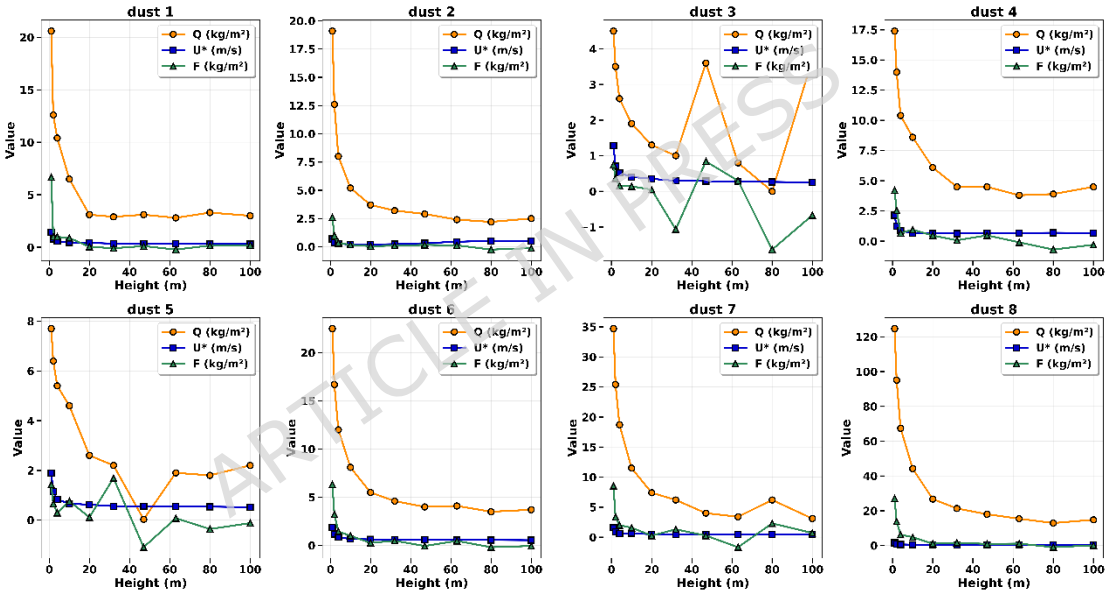

Figure 7. XT Vertical distribution characteristics of Q, F and U* under different dust processes

3.3 Multi-source remote sensing data combined with ground observations

After analyzing the influence of friction velocity on dust transport, this section will further explore the relationship between remote sensing data and ground observation data through aerosol optical depth (AOD) retrieval in combination with remote sensing data to supplement the limitations of ground monitoring.

The aerosol optical depth (AOD) retrieved by remote sensing can effectively reflect the atmospheric dust loading and shows a certain degree of correspondence with ground-based dust transport parameters. By comparing the MODIS AOD data from eight dust events with the measured horizontal

dust flux (Q), vertical dust flux (F), and friction velocity (U*) at the XT and TZ stations, notable differences were identified between the two sites.

At the XT station, the temporal variations in AOD generally exhibit a consistent pattern with the changes in Q, F, and U*, particularly during the more intense dust events. Periods characterized by enhanced near-surface wind strength and increased dust transport correspond to elevated AOD values, suggesting that local wind-blown sand activity plays a dominant role in contributing to the atmospheric dust column.

In contrast, at the TZ station, certain dust events display relatively high AOD values without a proportional increase in near-surface dust transport intensity. This discrepancy indicates that the atmospheric dust loading at TZ may be influenced not only by local surface emission but also by regional dust transport and upper-level dust recirculation processes. Similar patterns observed in multiple events further support the spatial heterogeneity in dust source contributions between the desert interior and the desert margin (see Figures 8 and 9).

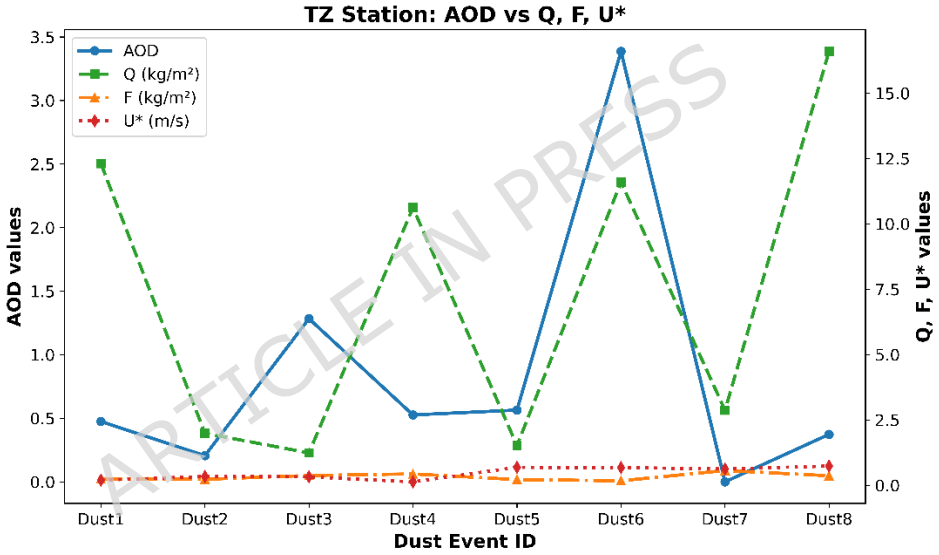

Figure 8. Corresponding relationship between AOD and dust flux Q, dust flux F and friction velocity U* at TZ station

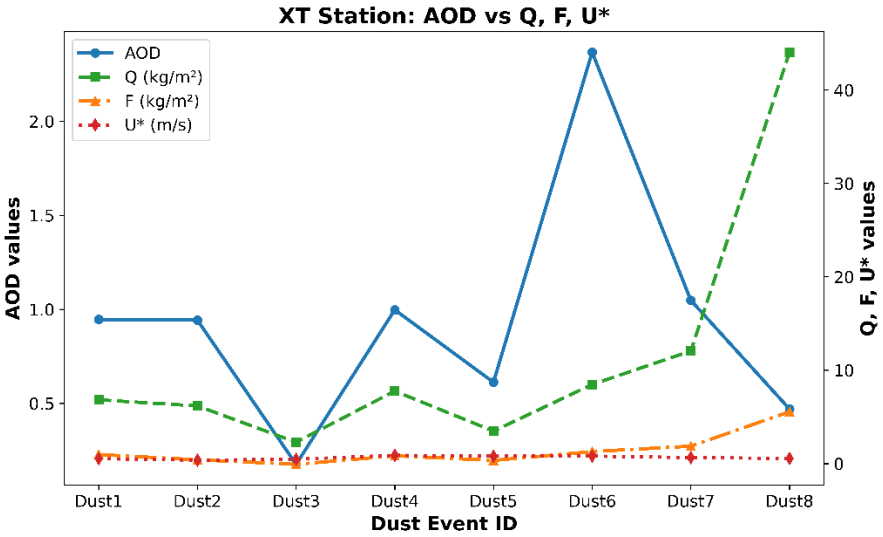

Figure 9. Relationship between AOD and dust flux Q, dust flux F and friction velocity U* at XT station

Correlation analysis between ground-level dust concentrations and Sentinel-5P AAI (Figure 10) shows a strong positive correlation at both stations (TZ: r = 0.96, p < 0.001; XT: r = 0.96, p < 0.001). This indicates that AAI can effectively capture the intensity of ground-level dust activity, particularly during strong dust events where surface and column measurements are highly synchronized.

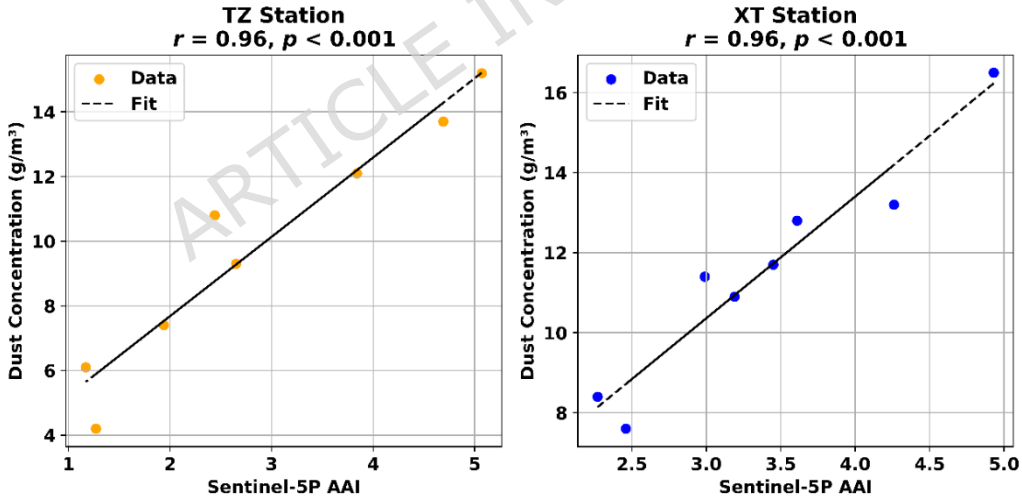

Figure 10. Relationship between Pearson correlation AAI and dust concentration

Figure 11 shows the height-resolved correlation between AAI and dust concentrations at TZ and XT stations. The two stations exhibit distinct vertical correlation patterns. At XT, AAI shows the strongest correlation with near-surface concentrations (1–10 m), peaking at 2 m (r = 0.928), with correlation gradually decreasing to 0.717 at 100 m. This suggests that at the desert margin, column-integrated absorbing aerosol is dominated by locally emitted dust. At TZ, correlation is lower in the near-surface layer (1–16 m, r ≈ 0.66) but increases at mid-altitudes (32–80 m), peaking at 47 m (r = 0.804). This

pattern indicates that in the desert interior, a significant portion of the absorbing aerosol column originates from elevated dust layers, consistent with regional transport or vertical mixing processes.

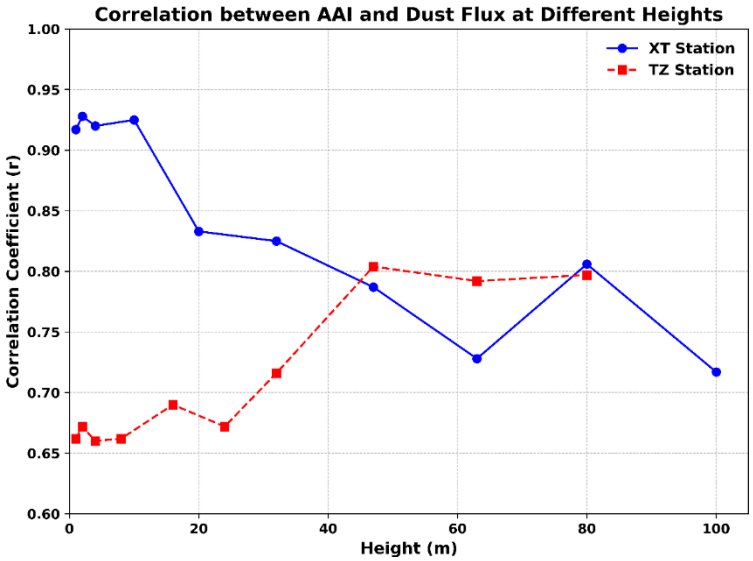

Figure 11. Pearson correlation between AAI and dust concentrations at various heights

4. Conclusion

At the Tazhong station (TZ):

A clear hierarchical relationship exists between particle size and dust flux. The horizontal flux (Q) generally decreases with increasing particle size, particularly at higher altitudes. Near the surface (1–2 m), higher concentrations of fine particles result in elevated Q values; with increasing height and particle size, both particle concentration and Q decline. During large-particle-dominated events (e.g., Dust 1 and Dust 8), D[4,3] is negatively correlated with Q, indicating that coarse particles are less favorable for long-distance horizontal transport. The vertical flux (F) also decreases significantly with increasing particle size. Due to their weak suspension capacity, coarse particles cannot maintain high concentrations aloft, leading to rapid attenuation of F with height, highlighting the dominant role of particle size in vertical transport efficiency.

Friction velocity (U*) shows an overall positive correlation with Q, indicating that stronger surface shear enhances particle entrainment and horizontal transport. However, the response of F to U* is inconsistent, showing only weak positive correlations in some events, suggesting that vertical transport is jointly controlled by particle size, gravitational settling, and turbulent structure. Both Q and U* decrease with height, exhibiting typical friction-layer characteristics, while F is concentrated in the lower layers and decays rapidly. This indicates that dust transport at TZ is constrained by limited vertical kinetic energy and relatively high settling rates. In addition, although high AOD values were observed during some events, corresponding

Q and F were not significant, implying that AOD at TZ is strongly influenced by regional transport or upper-level recirculation, with weak coupling to local dust emission.

The Sentinel-5P Aerosol Absorbing Index (AAI) shows a highly significant positive correlation with near-surface dust concentration ($r = 0.96$, $p < 0.001$), confirming its effectiveness in monitoring severe dust events. At TZ, the correlation is lower in the near-surface layer (1–16 m, ~0.66) and increases in the middle–upper layers (32–80 m), reaching 0.804, revealing distinct vertical variability.

At the Xiaotang station (XT):

The relationship between particle size and dust flux is more consistent, with fine particles dominating the transport process. Both Q and F increase as particle size decreases, and this trend is more pronounced at higher altitudes, indicating stronger vertical suspension capacity.

U* exhibits a significant positive correlation with Q, particularly during Dust 1, 2, 6, and 7. Although the correlation between F and U* is weaker, an overall increasing tendency is observed. Q is highest near the surface and decreases rapidly with height, while F peaks in the lower–middle layers, reflecting the nonlinear coupling among particle size, settling effects, and turbulent structure.

At XT, AOD shows good consistency with both Q and F, especially during Dust 6 and Dust 8, indicating strong local control of aeolian activity. AAI also exhibits a highly significant correlation with near-surface dust concentration ($r = 0.96$, $p < 0.001$). The correlation is strongest in the near-surface layer (1–10 m, $r > 0.91$) and gradually decreases with height, reaching 0.717 at 100 m.

Significant differences in dust transport mechanisms are observed between TZ and XT, reflecting the combined influence of topography, wind-field structure, and particle-size composition. The strong consistency between AAI and ground observations at both sites provides a reliable data foundation and methodological support for future multi-source data fusion in dust retrieval and early warning applications.

5. Discussion

This study systematically reveals the influence of key parameters for sandstorm initiation at the Taklamakan Desert's central station (TZ) and the desert-oasis transition zone at the Xiaotang station (XT) on dust flux. At the TZ station, the control of dust flux by particle size shows a clear vertical stratification: the horizontal flux Q decreases overall as particle size increases, and this trend becomes more pronounced with height. In the near-ground layer (1-2 meters), smaller particles accumulate, leading to an increase in Q, while at about 40 meters, the secondary sand initiation induced by topographic rise (local dunes) causes larger particles to be lifted again by local strong winds [10,44], resulting in a significant increase in D[4,3] (such as a 15 μm

increase during the dust 1 event). The combined effect of concentration attenuation causes Q to sharply decrease in the higher layers. The negative correlation between Q and D[4,3] during typical large particle events (such as dust 1 and dust 8) further supports the limitation of large particle sizes on horizontal transport distance [45]. The vertical flux F also decreases significantly with increasing particle size, especially near the 40-meter layer. Large particles lifted by secondary sand initiation have weak suspension ability and cannot maintain high-altitude concentration, causing a sharp decline in F above this height. The friction velocity U* has a clear positive effect on horizontal transport (Q is positively correlated with U* overall), but its impact on vertical flux F is weak (only showing a slight positive correlation in some events like dust 3 and dust 5), indicating that F is mainly constrained by a combination of particle size distribution, gravitational settling, and turbulent structure [46]. The rapid decay of Q and F in the vertical direction, combined with the decrease in U* from the lower to higher layers, collectively reflects the typical characteristics of the friction layer and the limitation of vertical kinetic energy on transport. It is worth noting that the station frequently experiences a decoupling phenomenon, where high AOD values coincide with low surface fluxes (Q, F) (for example, in dust 6, the AOD reached 3.39, yet Q and F did not increase synchronously). This suggests that the remote sensing signal is primarily dominated by regional transport or upper-air recirculation, and the contribution of local dust activity to AOD is relatively limited [47]. The AAI derived from Sentinel-5P inversion shows a strong ability to capture dust concentration [48], with the correlation between AAI and dust concentration peaking in the secondary sand source layer at 40 meters (32-80 meters) ($r = 0.304$), significantly higher than in the lower layers (1-16 meters, $r \approx 0.66$). This phenomenon directly confirms the prominent contribution of secondary sand initiation in topographic rise areas to aerosol column concentration in the middle to upper layers [44,49]. When strong winds pass over 40-meter high sand dunes, local wind speed acceleration and enhanced turbulence lead to the resuspension of sand particles, forming a region of exceptionally high dust concentration at specific heights, thereby significantly increasing the response sensitivity of AAI at this vertical level.

At the Xiaotang station, dust transport is dominated by small particle sizes. Both Q and F generally increase as particle size decreases, with a particularly strong vertical suspension and long-distance transport potential observed in the higher layers. The friction velocity U* significantly enhances horizontal transport, with a strong positive correlation between Q and U* in events such as dust 1, 2, 6, and 7, which aligns with classical sand and dust initiation theory. While F shows a weaker correlation with U*, it still exhibits a slight upward trend with increasing U* in multiple events, reflecting the indirect promoting effect of U* on vertical transport and the nonlinear coupling between particle size and turbulence. The peak value of Q is located near the surface and rapidly decreases with height, while F reaches its maximum in the middle to lower

layers. In terms of remote sensing response, the AOD at this station shows a high degree of synchronization with the surface fluxes (Q, F), particularly during dust 6 and dust 8 events, where AOD increases in tandem with Q and F. Combined with a significant increase in U*, this confirms a strong local control characteristic. The AAI is also strongly positively correlated with surface concentration ($r = 0.96$, $p < 0.001$), with the correlation being strongest in the near-surface layer (1-10 meters) ($r > 0.91$). The correlation decreases with height ($r = 0.717$ at 100 meters), which is consistent with the vertical distribution pattern of dust concentration, characterized by a "larger at the bottom and smaller at the top" profile.

The differences between the two stations profoundly reflect the coupling effects of local underlying surface properties and meteorological conditions: the sharply varying vertical gradient of particle size, complex topography (such as secondary sand sources), and limited vertical kinetic energy at the TZ station together constrain the transport efficiency. In contrast, the dominance of small particles, strong U* response, and relatively flat surface at the XT station favor efficient near-surface transport. Notably, the AAI at both stations shows a highly significant correlation with dust concentration ($r = 0.96$, $p < 0.001$), which validates the high applicability of Sentinel-5P in monitoring severe dust events and provides a solid data foundation for building dust warning models based on multi-source data fusion [50]. Future research should focus on the following directions: develop parameterization schemes for dust initiation and transport that integrate high-resolution terrain, surface roughness [51–53], and soil moisture data to enhance the simulation accuracy of models for regions with complex underlying surfaces. Conduct a systematic assessment of AAI vertical response characteristics across different regions (such as different sand source areas and transport path regions) to clarify how topographic uplift, boundary layer processes, and aerosol mixing states modulate the vertical representativeness of remote sensing signals [54,55]. This will provide theoretical support for remote sensing validation of global dust models. Investigate the formation mechanisms of secondary sand sources and their impact on the vertical distribution of dust. Combining meteorological factors will help enhance the understanding of complex dust transport processes and improve the accuracy of remote sensing inversion. Additionally, some studies suggest that comparing MODIS AOD with ground-based flux observations can reveal the characteristics of dust transport in different regions [56–60]. In certain areas, AOD shows a highly consistent trend with surface dust flux intensity, particularly when surface dust concentrations increase and AOD rises synchronously, indicating a strong local response [61,62]. However, in some areas, despite observing higher AOD, the surface flux and friction velocity did not change significantly, suggesting that exogenous dust or upper-air recirculation may be the dominant factors [63–65]. Additionally, some studies indicate that the topographic fluctuations significantly influence the wind field and dust transport pathways, affecting

the distribution of dust concentrations at different altitudes [10,63,66,67], especially in areas with secondary sand sources. These studies provide new insights into the complexity of dust transport and emphasize the close relationship between topography, meteorological conditions, and remote sensing data interpretation. Such research will significantly enhance the understanding of dust transport complexities and provide technological support for ecological safety in arid regions and precise control of dust disasters.

5.1 Study Limitations

Despite the robust integration of ground-based observations and multi-source remote sensing data, several limitations should be acknowledged. First, spatial scale mismatch remains an inherent challenge. Ground-based measurements represent point-scale observations, whereas satellite products such as MODIS AOD and Sentinel-5P AAI are derived from pixel-averaged signals, which may include contributions from regional transport and upper-level aerosols. This mismatch can weaken the direct coupling between surface dust flux and remotely sensed aerosol signals, particularly in the desert interior.

Satellite observations are limited by temporal sampling. Daily overpass frequency may fail to capture short-lived or highly localized dust emission events driven by transient wind bursts. Third, uncertainties associated with retrieval algorithms, cloud contamination, and surface reflectance over bright desert surfaces can introduce additional errors in satellite-derived products.Finally, while AAI demonstrates strong potential in reflecting dust vertical structure, it remains an indirect indicator of aerosol loading and cannot fully resolve detailed vertical profiles without auxiliary information. Future studies should integrate higher temporal resolution satellite observations, lidar-based vertical profiling, and numerical modeling to further improve the representation of dust emission and transport processes.

CRediT authorship contribution statement

Mayibaier Maihamuti: Conceptualization, Writing – original draft, Formal Analysis.
Wen Huo: Methodology, Supervision, Writing – review & editing.
Yongqiang Liu: Validation.
Yifei Wang: Investigation, Data Curation.
Fan Yang: Experimental Design, Supervision.
Chenglong Zhou, Xinghua Yang, Ali Mamtimin: Investigation, Data Curation.
Mierxiatijiang Maihemuti: Visualization

Declaration of competing interest

The authors declare no competing interests.

Funding: This research was funded by the Tianshan Talent Project of Xinjiang (Grant No. 2023TSYCCX0075), China Meteorological Administration Youth Innovation Team Project (CMA2024QN13); and the Xinjiang Science and Technology Innovation Team (Tianshan Innovation Team) Project (2022TSYCTD0007).

Data Availability Statement: The MODIS aerosol optical depth (AOD) data used in this study were obtained from the NASA LAADS DAAC, and the Sentinel-5P aerosol absorbing index (AAI) data were provided by the ESA Copernicus Programme. These satellite datasets are publicly available.The ground-based dust horizontal transport flux (Q), vertical dust flux (F), multi-level wind, and meteorological observations were obtained from in situ field experiments conducted by the authors at the Taklimakan Desert Meteorological National Field Science Observation and Research Station. Due to the site-specific nature of the observation stations and the experimental characteristics of the datasets, these ground-based data are not publicly available but can be obtained from the corresponding authors upon reasonable request.

Acknowledgements

This research was funded by the Tianshan Young Talents Program of Xinjiang (Project No. 2023TSYCCX0075), the China Meteorological Administration's Young Innovative Team Project (Project No. CMA2024QN13), and the Tianshan Innovation Team Project of Xinjiang Science and Technology Innovation Team Program (Project No. 2022TSYCTD0007). We would like to thank the Desert Meteorological Institute of the China Meteorological Administration (Urumqi) for providing critical datasets. We also thank the School of Geography and Remote Sensing Science, Xinjiang University (Urumqi), for their technical support. Due to the station-specific nature of ground observation data, it is not publicly available but can be reasonably requested from the corresponding author. We appreciate the NASA LAADS DAAC data center (https://ladsweb.modaps.eosdis.nasa.gov) for providing MODIS data. We also thank the European Space Agency (ESA) Copernicus Program for providing Sentinel-5P data.

References

1. Zucca, C., Fleiner, R., Bonaiuti, E. & Kang, U. Land degradation drivers of anthropogenic sand and dust storms. *CATENA* **219**, 106575 (2022).
2. Sun, H., Liu, X. & Wang, A. Seasonal and interannual variations of atmospheric dust aerosols in mid and low latitudes of Asia – A comparative

study. *Atmospheric Research* **244**, 105036 (2020).

3. Lee, Y. C., Yang, X. & Wenig, M. Transport of dusts from East Asian and non-East Asian sources to Hong Kong during dust storm related events 1996–2007. *Atmospheric Environment* **44**, 3728–3738 (2010).
4. Biagio, C. D., Banks, J. R. & Gaetani, M. Dust atmospheric transport over long distances. in *Reference Module in Earth Systems and Environmental Sciences* (2021). doi:10.1016/B978-0-12-818234-5.00033-X.
5. Hu, Z. *et al.* Modeling dust sources, transport, and radiative effects at different altitudes over the Tibetan Plateau. *Atmospheric Chemistry and Physics* **20**, 1507–1529 (2020).
6. Middleton, N. J. Desert dust hazards: A global review. *Aeolian Research* **24**, 53–63 (2017).
7. Peng, L., Wan, Y., Shi, H., Anwaier, A. & Shi, Q. Influence of Climate, Topography, and Hydrology on Vegetation Distribution Patterns—Oasis in the Taklamakan Desert Hinterland. *Remote Sensing* **15**, 5299 (2023).
8. Wei, G. *et al.* Grain-size composition of the surface sediments in Chinese deserts and the associated dust emission. *CATENA* **219**, 106615 (2022).
9. Raffaele, L., Bruno, L. & Wiggs, G. F. S. Uncertainty propagation in aeolian processes: From threshold shear velocity to sand transport rate. *Geomorphology* **301**, 28–38 (2018).
10. Huo, W. *et al.* Influence of Topographic Relief on Sand Transport in the Near-Surface Layer During Dust Storms in the Taklimakan Desert. *Front. Environ.*

Sci. **10**, (2022).

11. Marticorena, B. Dust Production Mechanisms. in *Mineral Dust: A Key Player in the Earth System* (eds Knippertz, P. & Stuut, J.-B. W.) 93–120 (Springer Netherlands, Dordrecht, 2014). doi:10.1007/978-94-017-8978-3_5.
12. Zhao, H., Balbo, A., Brown, P. H. & Schuck, P. The boundary structure in the analysis of reversibly interacting systems by sedimentation velocity. *Methods* **54**, 16–30 (2011).
13. Du, H. *et al.* Modeling dust emission in alpine regions with low air temperature and low air pressure – A case study on the Qinghai-Tibetan Plateau (QTP). *Geoderma* **422**, 115930 (2022).
14. Dupont, S. Scaling of Dust Flux With Friction Velocity: Time Resolution Effects. *Journal of Geophysical Research: Atmospheres* **125**, e2019JD031192 (2020).
15. Meng, Y., Huang, N., Zhang, C. & Dun, H. Mechanics of wind erosion-induced dust emission from soil crusts: A theoretical predictive model. *CATENA* **246**, 108342 (2024).
16. Lyu, P. *et al.* Research on remote sensing prospecting technology based on multi-source data fusion in deep-cutting areas. *Ore Geology Reviews* **138**, 104359 (2021).
17. Song, Q., Zhang, Z., Yu, H., Ginoux, P. & Shen, J. Global dust optical depth climatology derived from CALIOP and MODIS aerosol retrievals on decadal timescales: regional and interannual variability. *Atmospheric Chemistry and*

Physics **21**, 13369–13395 (2021).

18. Guehaz, R., Sivakumar, V. & Mbatha, N. A case study on the dust storm that occurred on March 13–18, 2022, over the Algerian Sahara, using satellite remote sensing. *Journal of Atmospheric and Solar-Terrestrial Physics* **264**, 106345 (2024).
19. Wielicki, B. A. & Parker, L. On the determination of cloud cover from satellite sensors: The effect of sensor spatial resolution. *Journal of Geophysical Research: Atmospheres* **97**, 12799–12823 (1992).
20. Xie, Y. *et al.* The influence of cloud cover on the reliability of satellite-based solar resource data. *Renewable and Sustainable Energy Reviews* **208**, 115070 (2025).
21. Lee, C. A., Gasster, S. D., Plaza, A., Chang, C.-I. & Huang, B. Recent Developments in High Performance Computing for Remote Sensing: A Review. *IEEE Journal of Selected Topics in Applied Earth Observations and Remote Sensing* **4**, 508–527 (2011).
22. Liang, S. *et al.* Advancements in high-resolution land surface satellite products: A comprehensive review of inversion algorithms, products and challenges. *Science of Remote Sensing* **10**, 100152 (2024).
23. Wang, L., Ma, Y., Yan, J., Chang, V. & Zomaya, A. Y. pipsCloud: High performance cloud computing for remote sensing big data management and processing. *Future Generation Computer Systems* **78**, 353–368 (2018).
24. Xiong, Z., Xu, X., Yang, Y. & Luo, T. Diurnal vertical distribution and transport

of dust aerosol over and around Tibetan Plateau from lidar on International Space Station. *Atmospheric Research* **294**, 106939 (2023).

25. Fania, A. *et al.* Estimation of Daily Ground Level Air Pollution in Italian Municipalities with Machine Learning Models Using Sentinel-5P and ERA5 Data. *Remote Sensing* **16**, 1206 (2024).
26. Li, M. & Yao, J. Precipitation extremes observed over and around the Taklimakan Desert, China. *PeerJ* **11**, e15256 (2023).
27. Yang, X., Liu, Z., Zhang, F., White, P. D. & Wang, X. Hydrological changes and land degradation in the southern and eastern Tarim basin, Xinjiang, China. *Land Degradation & Development* **17**, 381–392 (2006).
28. Spengler, R. N. *Fruit from the Sands: The Silk Road Origins of the Foods We Eat*. (Univ of California Press, 2020).
29. Prudnikova, T. N. The Tarim Basin and the Transformation of its Landscapes. *Arid Ecosyst* **9**, 157–165 (2019).
30. Zheng, Z. *et al.* Studies on the Correlation between δ13C and Nutrient Elements in Two Desert Plants. *Forests* **14**, (2023).
31. Jin, L. & He, Q. On the Association between Fine Dust Concentrations from Sand Dunes and Environmental Factors in the Taklimakan Desert. *Remote Sensing* **15**, 1719 (2023).
32. Wenzhang, M., Jin, Y., Sirui, D., Changqing, S. & Tingning, Z. Spatial and Temporal Variation Characteristics of Wind Erosion Climate Erosivity in the Arid Desert Region of Northwestern China. *Journal of Resources and Ecology*

14, (2023).

33. Liu, X., Kang, Y., Chen, H. & Lu, H. Comparison of surface wind speed and wind speed profiles in the Taklimakan Desert. *PeerJ* **10**, e13001 (2022).
34. Guo, X., Zhu, L., Yang, Z., Yang, C. & Li, Z. Spatial–Temporal Changes in the Distribution of Populus euphratica Oliv. Forests in the Tarim Basin and Analysis of Influencing Factors from 1990 to 2020. *Forests* **15**, 1384 (2024).
35. Yang, X. *et al.* Spatial and temporal variations of blowing dust events in the Taklimakan Desert. *Theor Appl Climatol* **125**, 669–677 (2016).
36. Gillette, D. A. & Passi, R. Modeling dust emission caused by wind erosion. *Journal of Geophysical Research: Atmospheres* **93**, 14233–14242 (1988).
37. Nickling, W. G. & Gillies, J. A. Dust emission and transport in Mali, West Africa. https://onlinelibrary.wiley.com/doi/10.1111/j.1365-3091.1993.tb01365.x.
38. Sow, M., Alfaro, S. C., Rajot, J. L. & Marticorena, B. Size resolved dust emission fluxes measured in Niger during 3 dust storms of the AMMA experiment. *Atmospheric Chemistry and Physics* **9**, 3881–3891 (2009).
39. Monin, A. S. & Obukhov, A. M. Basic laws of turbulent mixing in the surface layer of the atmosphere.
40. *An Introduction to Boundary Layer Meteorology*. (Springer Netherlands, Dordrecht, 1988). doi:10.1007/978-94-009-3027-8.
41. Garratt, J. R. *The Atmospheric Boundary Layer*. (Cambridge ; New York : Cambridge University Press, 1992).
42. Businger, J. A., Wyngaard, J. C., Izumi, Y. & Bradley, E. F. Flux-Profile

Relationships in the Atmospheric Surface Layer. *Journal of the Atmospheric Sciences* **28**, 181–189 (1971).

43. Dyer, A. J. A review of flux-profile relationships. *Boundary-Layer Meteorol* **7**, 363–372 (1974).
44. Maihamuti, M. *et al.* Research on Key Sand Generating Parameters and Remote Sensing Traceability of Dust Storms in the Taklamakan Desert. *Remote Sensing* **17**, 1870 (2025).
45. Bagnold, R. A. The Movement of Desert Sand. *The Geographical Journal* **85**, 342–365 (1935).
46. Whicker, J. J., Breshears, D. D. & Field, J. P. Progress on relationships between horizontal and vertical dust flux: Mathematical, empirical and risk-based perspectives. *Aeolian Research* **14**, 105–111 (2014).
47. Gui, K. *et al.* Record-breaking dust loading during two mega dust storm events over northern China in March 2021: aerosol optical and radiative properties and meteorological drivers. *Atmospheric Chemistry and Physics* **22**, 7905–7932 (2022).
48. Hassaan, M. A., Abdallah, S. M., Shalaby, E.-S. A. & Ibrahim, A. A. Assessing vulnerability of densely populated areas to air pollution using Sentinel-5P imageries: a case study of the Nile Delta, Egypt. *Sci Rep* **13**, 17406 (2023).
49. Lei, L. *et al.* Vertical Distributions of Primary and Secondary Aerosols in Urban Boundary Layer: Insights into Sources, Chemistry, and Interaction with Meteorology. *Environ. Sci. Technol.* **55**, 4542–4552 (2021).

50. Guehaz, R., Sivakumar, V. & Mbatha, N. A case study on the dust storm that occurred on March 13–18, 2022, over the Algerian Sahara, using satellite remote sensing. *Journal of Atmospheric and Solar-Terrestrial Physics* **264**, 106345 (2024).

51. Mejia, J. F., Gillies, J. A., Etyemezian, V. & Glick, R. A very-high resolution (20m) measurement-based dust emissions and dispersion modeling approach for the Oceano Dunes, California. *Atmospheric Environment* **218**, 116977 (2019).

52. Leung, D. M. *et al.* A new process-based and scale-aware desert dust emission scheme for global climate models – Part I: Description and evaluation against inverse modeling emissions. *Atmospheric Chemistry and Physics* **23**, 6487–6523 (2023).

53. Zheng, Z., Du, S., Taubenböck, H. & Zhang, X. Remote sensing techniques in the investigation of aeolian sand dunes: A review of recent advances. *Remote Sensing of Environment* **271**, 112913 (2022).

54. Liu, Y., Huang, J. & Huang, F. A Comprehensive Review on Study Methods of Aerosol Optical Properties in Different Dimensions. *IEEE Access* **11**, 36763–36786 (2023).

55. Kotthaus, S. *et al.* Atmospheric boundary layer height from ground-based remote sensing: a review of capabilities and limitations. *Atmospheric Measurement Techniques* **16**, 433–479 (2023).

56. Ma, X., Bartlett, K., Harmon, K. & Yu, F. Comparison of AOD between

CALIPSO and MODIS: significant differences over major dust and biomass burning regions. *Atmospheric Measurement Techniques* **6**, 2391–2401 (2013).

57. Vijayakumar, K., Devara, P. C. S., Rao, S. V. B. & Jayasankar, C. K. Dust aerosol characterization and transport features based on combined ground-based, satellite and model-simulated data. *Aeolian Research* **21**, 75–85 (2016).
58. Chen, S. *et al.* Emission, transport, and radiative effects of mineral dust from the Taklimakan and Gobi deserts: comparison of measurements and model results. *Atmospheric Chemistry and Physics* **17**, 2401–2421 (2017).
59. Song, Q., Zhang, Z., Yu, H., Ginoux, P. & Shen, J. Global dust optical depth climatology derived from CALIOP and MODIS aerosol retrievals on decadal timescales: regional and interannual variability. *Atmospheric Chemistry and Physics* **21**, 13369–13395 (2021).
60. Merdji, A. B., Lu, C., Xu, X. & Mhawish, A. Long-term three-dimensional distribution and transport of Saharan dust: Observation from CALIPSO, MODIS, and reanalysis data. *Atmospheric Research* **286**, 106658 (2023).
61. Badarinath, K. V. S. *et al.* Long-range transport of dust aerosols over the Arabian Sea and Indian region — A case study using satellite data and ground-based measurements. *Global and Planetary Change* **72**, 164–181 (2010).
62. Chen, Z., Gao, X. & Lei, J. Dust emission and transport in the Aral Sea region.

Geoderma **428**, 116177 (2022).

63. Hu, Z. *et al.* Modeling dust sources, transport, and radiative effects at different altitudes over the Tibetan Plateau. *Atmospheric Chemistry and Physics* **20**, 1507–1529 (2020).
64. Wang, T. *et al.* Identifying a transport mechanism of dust aerosols over South Asia to the Tibetan Plateau: A case study. *Science of The Total Environment* **758**, 143714 (2021).
65. Dong, Z. *et al.* Aeolian dust transport, cycle and influences in high-elevation cryosphere of the Tibetan Plateau region: New evidences from alpine snow and ice. *Earth-Science Reviews* **211**, 103408 (2020).
66. Silvester, S. A., Lowndes, I. S. & Hargreaves, D. M. A computational study of particulate emissions from an open pit quarry under neutral atmospheric conditions. *Atmospheric Environment* **43**, 6415–6424 (2009).
67. Zhai, L. *et al.* Dynamic effects of topography on dust particles in the Beijing region of China. *Atmospheric Environment* **213**, 413–423 (2019).